Confining calcium oxalate crystal growth in a carbonated apatite-coated microfluidic channel to better understand the role of Randall's plaque in kidney stone formation

Samantha Bourg, Karol Rakotozandriny, Ivan T. Lucas, Emmanuel Letavernier, Christian Bonhomme, Florence Babonneau, Ali Abou-Hassan

Confining calcium oxalate crystal growth in a carbonated apatite-coated microfluidic channel to better understand the role of Randall's plaque in kidney stone formation†

Samantha Bourg,[a] Karol Rakotozandriny,[ab] Ivan T. Lucas,[c] Emmanuel Letavernier,[d] Christian Bonhomme,[b] Florence Babonneau[b] and Ali Abou-Hassan*[ae]

Effective prevention of recurrent kidney stone disease requires the understanding of the mechanisms of its formation. Numerous *in vivo* observations have demonstrated that a large number of pathological calcium oxalate kidney stones develop on an apatitic calcium phosphate deposit, known as Randall's plaque. In an attempt to understand the role of the inorganic hydroxyapatite phase in the formation and habits of calcium oxalates, we confined their growth under dynamic physicochemical and flow conditions in a reversible microfluidic channel coated with hydroxyapatite. Using multi-scale characterization techniques including scanning electron and Raman microscopy, we showed the successful formation of carbonated hydroxyapatite as found in Randall's plaque. This was possible due to a new two-step flow seed-mediated growth strategy which allowed us to coat the channel with carbonated hydroxyapatite. Precipitation of calcium oxalates under laminar flow from supersaturated solutions of oxalate and calcium ions showed that the formation of crystals is a substrate and time dependent complex process where diffusion of oxalate ions to the surface of carbonated hydroxyapatite and the solubility of the latter are among the most important steps for the formation of calcium oxalate crystals. Indeed when an oxalate solution was flushed for 24 h, dissolution of the apatite layer and formation of calcium carbonate calcite crystals occurred which seems to promote calcium oxalate crystal formation. Such a growth route has never been observed *in vivo* in the context of kidney stones. Under our experimental conditions, our results do not show any direct promoting role of carbonated hydroxyapatite in the formation of calcium oxalate crystals, consolidating therefore the important role that macromolecules can play in the process of nucleation and growth of calcium oxalate crystals on Randall's plaque.

Introduction

The prevalence and recurrence rates of nephrolithiasis increase every year, more specifically in the industrialized population.[1]

The majority of kidney stones (KSs) are composed of calcium oxalates (CaOx) that form by heterogeneous nucleation on calcium phosphate (CaP) deposits.[2–4] Tiselius[5] discussed two possible routes for the formation of CaP crystals: an interstitial route in which the CaP material is internalized by tubular cells, leading to the formation of sub-epithelial plaques at the tip of the renal papillae known as Randall's plaques (RPs)[6] and an intratubular route for which CaP precipitates are transported downwards with the urine stream in the direction towards the collecting duct and the caliceal space.[7–9] It was reported that RP is more pronounced in idiopathic hypercalciuric stone formers,[4] and also that

[a] *Laboratoire Physicochimie des Electrolytes et Nanosystèmes Interfaciaux (PHENIX), CNRS, Sorbonne Université, UMR 8234, Campus Jussieu, 4 place Jussieu, F-75005 Paris, France. E-mail: Ali.abou_hassan@sorbonne-universite.fr*
[b] *Laboratoire de Chimie de la Matière Condensée de Paris (LCMCP), CNRS, Sorbonne Université, UMR 7574, Campus Jussieu, 4 place Jussieu, F-75005 Paris, France*
[c] *Laboratoire Interfaces et Systèmes Electrochimiques (LISE), CNRS, Sorbonne Université, UMR 8235, Campus Jussieu, 4 place Jussieu, F-75005 Paris, France*
[d] *AP-HP, Hôpital Tenon, Explorations Fonctionnelles Multidisciplinaires et Laboratoire des Lithiases, F-75020 Paris, France*
[e] *Institut Universitaire de France (IUF), 75231 Paris Cedex 05, France*

both hyperoxaluria and hypercalciuria lead to the formation of intratubular rather than interstitial deposits.[10]

The main inorganic component of RP is carbonated hydroxyapatite (CHA) and amorphous calcium phosphate mixed with an organic matrix that is rich in proteins, glycosaminoglycans and lipids, as well as collagen fibers.[3,9,11–13]

Several studies have investigated the formation of RP and the role it plays in the nucleation of CaOx stones, and a recent update has been published.[4] Xie *et al.*[14] proposed a phase transformation from amorphous CaOx clusters (known to be potential intermediates in biomineralization)[15] to multicrystal aggregates promoted by amorphous calcium phosphate (ACP) complexes. The role of pH in the dissolution of CaP crystals and the release of Ca^{2+} ions has also been highlighted as an important factor in the formation of CaOx on RP.[5] Moreover, studies of the interfaces between CaOx stones and RP have brought further support for the role of RP as a nucleus in the heterogeneous nucleation process of CaOx crystals.[5,16,17] Scanning electron microscopy (SEM) studies detailed the organization of RP in microspherules attached to COM crystals.[2,3,16,18] Assumptions have been formulated to explain the formation of CaOx stones from RP as a final response to: (i) high urine calcium concentration, (ii) reduced urine volume and (iii) decreased pH leading to loss of papillary epithelial integrity.[5,18,19] However, to date, the mechanism of KS formation from RP is still an open debate and different questions remain on the role of RP including the role of the apatite phase in the formation and crystal habits of CaOx. In fact, KS formation occurs in a very complex dynamic chemical and flow environment whose characteristics are difficult, if not impossible, to fully reproduce *in vitro*. However a suitable model for CaOx crystal growth, which could even partially mimic these conditions, would certainly contribute to a better understanding of *ex vivo* observations.

Microscale fluidic devices are suitable *in vitro* systems for reproducing a 3D microenvironment mimicking nephrons.[20–22] Our team has previously studied CaOx precipitation after co-mixing of supersaturated calcium and oxalate aqueous solutions using a microfluidic platform under physicochemical conditions mimicking those of pathological CaOx KS formation in a nephron collecting duct.[23–25] CaOx stones exhibit two crystalline phases, the more thermodynamically stable monohydrate whewellite ($CaC_2O_4{\cdot}H_2O$, COM) and the dihydrate weddellite ($CaC_2O_4{\cdot}2H_2O$, COD). The identification of CaOx crystals by scanning electron microscopy (SEM) and Raman scattering was made possible thanks to the reversible magnetic sealing system of the microfluidic cell; we were able to show the preferential precipitation of COM crystals in a boat-like shape in agreement with *in vivo* observations.[24] Other teams have more specifically studied the influence of the presence of CaP on the overgrowth of CaOx KSs using fluidic devices. Indeed, Gombedza *et al.*[26] developed a Y-shaped microchannel covered with kidney cells to mimic the existing microenvironment for the growth of mixed CaOx/CaP crystals in the proximal tubule of nephrons. More recently, Kuliasha *et al.*[27] reported the development of an easy-to-use millifluidic platform based on basement membrane extract (BME) as a biologically relevant crystallization substrate to explore the *in situ* growth of CaOx crystals in the presence of a synthetic RP and urinary inhibitors (citrate, magnesium ions and osteopontin). This study followed a prior study by the same group on the development of a biomimetic model of RP based on the mineralization of decellularized tissues.[28,29] In the flow-cell crystallization study,[27] the authors suggested that the BME substrate and the urinary inhibitors play a major role in the control of the crystal nucleation and growth, compared to the CaP surface. However, they did not succeed in forming a CaP layer in the channel without the BME, and thus could not assess the role of CaP in the absence of organic components. The millienvironment in this study did not reproduce well the microconfinement in the renal tissues (≈100 μm). Also, in these previous studies, the formation of CaP required the presence of an organic substrate (proteins, cells) which allowed the growth of CaP from solution or its attachment from preformed CaP seeds. To date, the successful formation of a carbonated mimetic CaP layer in a confined channel, as encountered in RP, with no organic matrix has never been reported. Finally, none of these reports have provided multi-scale characterization of the precipitated crystals, because of the irreversibility of the systems. Considering that RP is mostly composed of inorganic phases, engineering a carbonated apatite structure confined in a microchannel and subjected to dynamic physicochemical conditions should provide an opportunity to better understand the role of the inorganic component of RP in the crystallization (formation, habits) of CaOx.

In a novel innovative and versatile methodology based on microfluidics, our work proposes as a first step a simplified model to study the effect of apatite, the major component of RP, on CaOx crystallization while considering important parameters to mimic *in vivo* conditions such as the physiological, dynamic (physicochemical and hydrodynamic) and confinement conditions. We also describe a safe, easy and reproducible process for coating the inner surface of the microchannel with CHA based on a new flow seed-mediated growth approach. Subsequently, an aqueous oxalate solution was infused alone or co-mixed with an aqueous calcium solution at the slower total flow rate accessible with the syringe pumps (≈10 times the physiological flow in one collecting duct) to approach flow physiological conditions.[30] The concentrations in oxalate and calcium ions that have been used throughout this study correspond to moderate hyperoxaluria ($[Ox^{2-}]$ = 0.4 mM) and pathological hypercalciuria ($[Ca^{2+}]$ = 12.0 mM), respectively. Thanks to the sealing reversibility of the microfluidic device, *ex situ* and multiscale characterization including optical microscopy,

SEM coupled to energy-dispersive X-ray spectroscopy (SEM-EDX) and Raman microscopy could be used on the one hand to optimize CHA coating and on the other hand to study its impact on the formation and crystal habits of CaOx crystals.

Materials and methods

Chemicals

A polydimethylsiloxane (PDMS) kit (Sylgard 184) was purchased from Dow Corning. Iron pentacarbonyl powder was purchased from Neochimie. Sodium chloride (NaCl) was purchased from Carlo Erba. Potassium chloride (KCl) was purchased from Acros Organics. Sodium bicarbonate ($NaHCO_3$), magnesium chloride hexahydrate ($MgCl_2{\cdot}6H_2O$), calcium chloride ($CaCl_2$), anhydrous di-potassium hydrogen phosphate (K_2HPO_4), sodium sulfate (Na_2SO_4), hydrochloric acid (37%), nitric acid (67%) and Trizma® base ($NH_2C(CH_2OH)_3$) were purchased from Sigma Aldrich and used without any further purification.

Microfabrication of the microfluidic platform

The microfabrication of the device was adapted from our previous publication.[24] A Y-shaped microchannel of 100 μm in height and width and 2.5 cm in length was designed with 3D CAO software Inventor® (Autodesk). The design was then transposed on a brass mold (0.5 × 8.0 × 8.0 cm) by micromachining (Minitech®) at Pierre-Gilles de Gennes Institute (Paris, France). Afterwards, magnetic PDMS was prepared by mixing the silicone elastomer with iron carbonyl powder and the curing agent in a 10 : 10 : 1 weight ratio. The black viscous mixture was poured onto the brass mold and the air bubbles were removed under vacuum. The magnetic PDMS was heated at 70 °C for 2 h and after curing, the microchannel was peeled off the mold and holes were drilled in the reservoirs with a 0.5 mm punch (Harris Uni Core). Prior to the CaP deposit, a glass coverslip (24 × 60 mm, VWR) was pretreated with dioxygen (O_2) plasma (10 sccm of O_2, 90 W, 5 min, Electronic Diener, Femto) before assembling the microfluidic device. For the other experiments, the glass coverslip was just rinsed with ethanol and ultrapure water. All experiments were performed with the glass coverslip on top of the microfluidic platform which was sealed with magnets.

Hydroxyapatite deposition through a flow seed-mediated growth method

The two-step procedure to deposit HA on the inner surface of the assembled microchannel was adapted from Liu *et al.*[31] (see ESI,† Table S1) and is presented in Fig. 1. 20.0 mM calcium chloride prepared with Tris-HCl buffer (10.0 mM, pH 7.4) and 12.0 mM di-potassium hydrogen phosphate prepared with ultrapure water were first infused through the two inlets at the same flow rate (Q_i) (1.0 μL min^{-1}) (*i.e.* Q_{tot} = 2.0 μL min^{-1}) at 37 °C (seeding step). The nucleation of CaP depends largely on the time of infusion of the two precursor solutions;[32] three infusion times (15 min, 30 min and 1 h 30 min) were tested and 1 h 30 was selected as the best condition. In the second step, a solution with ionic concentration 1.5 times greater than the classical simulated body fluid solution (1.5 SBF)[33] was infused at 37 °C for 18 h at Q_i = 1.0 μL min^{-1} (*i.e.* Q_{tot} = 2.0 μL min^{-1}) to promote the growth of the biomimetic apatite coating.[30,34,35] The 1.5 SBF solution (chemical composition given in ref. 32) was prepared with Tris-HCl buffer (10.0 mM, pH 7.4). Finally, the assembled microchannel was then washed by injecting ultrapure water for 10 min at Q_{tot} = 2.0 μL min^{-1}.

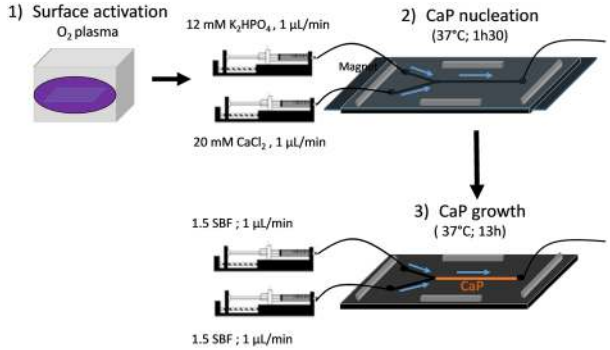

Fig. 1 Experimental procedure used for the 2-step flow seed-mediated growth deposition of HAp on the inner surfaces of the microchannel composed of magnetic PDMS on the bottom side and a glass coverslip on the top side (100 × 100 μm × 2.5 cm). The blue arrows indicate the fluid flow direction.

Formation of CaOx crystals

The calcium chloride (12.0 mM) and sodium oxalate (0.4 mM) solutions prepared with ultrapure water or the sodium oxalate solution alone were introduced with the same flow rate (*i.e.* Q_i = 0.1 μL min^{-1}) into the microchannel coated, or not, with HA.

Characterization

The phases and the morphologies of CaP and CaOx crystals were identified by optical microscopy (Leica, 5× magnification), Raman microscopy (LabRAM HR Evolution, Horiba), SEM-EDX (Hitachi S-3400) and SEM-FEG (Hitachi SU-70). The thickness of the CaP coating on the glass coverslip was measured by SEM-FEG (45° tilt) after scratching it with a scalpel tip. Prior to the characterization by SEM-FEG, the microchannel was washed with ultrapure water with a flow rate of 2.0 μL min^{-1} for 10 min and unsealed and the sample was left to dry. This was followed by 2 nm platinum coating using a Polaron E5100 sputter-coater (Polaron Equipment, Watford, Hertfordshire, UK).

The crystals obtained from droplets (total volume of about 24 μL) collected at the end of the microchannel were observed by SEM-FEG (Hitachi SU-70) after drying at room temperature on a clean glass lamella. The concentration of calcium in the droplets at the exit of the microchannel was

measured by atomic absorption spectroscopy using a Perkin Elmer AAnalyst 100.

Results and discussion

Formation of the hydroxyapatite coating

To mimic the inorganic component of RP, the CaP coating was first deposited on the internal surface of the microchannel (Fig. 1) and then washed under water flow. An SBF-based solution was used to ensure that the final CaP composition was close to that of a biomimetic apatite. The coating on the glass coverslip was characterized by optical microscopy (Fig. 2a), SEM-FEG (Fig. 2b and c), SEM-EDX (Fig. 2d) and Raman spectroscopy (Fig. 2e). The contrast observed all along the microchannel by optical microscopy (Fig. 2a) suggests the presence of a coating whose well-defined microstructure is revealed by SEM imaging (Fig. 2b). Its thickness is around 600 ± 100 nm (Fig. 2c). EDX element mapping confirmed the presence of CaP (Fig. 2d) with a homogeneous distribution of Ca and P ions at the surface and the removal of NaCl crystals, largely present before the washing step. The resulting microstructure of the coating presents an alveolar morphology (Fig. 2b). Although studies on *in situ* synthesis of CaP under flow in microchannels have already been reported, SEM images of the coatings were not shown due to the irreversibility of the channel.[32] The coating morphology is very similar to what has already been obtained by Kuliasha *et al.*[27] in a millifluidic channel. In this work, they already noticed that the overall morphology was different from the usual CaP spherules seen at the surface of RP.[2,3,16,18] Interestingly, Daudon *et al.*[3] stated that the carbonated hydroxyapatite based stones are made of needles aggregated as spherulites, but that in contrast, the interface between RP and the CaOx crystals does not show crystals, but rather a smooth interface, suggesting the presence of an amorphous material (either amorphous CaP and/or proteins). The morphology shown in Fig. 2c could therefore be considered close to that observed for CaP in RP.

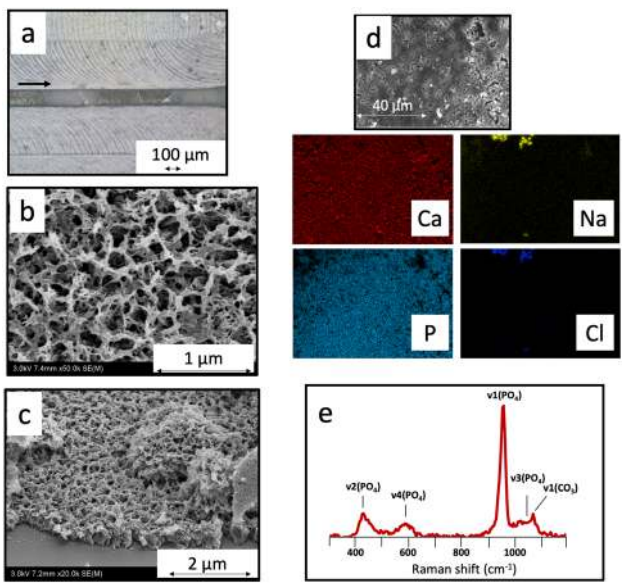

Fig. 2 CaP coating in the microchannel. a) Optical micrograph; b and c) SEM-FEG micrographs of the coated glass coverslip; d) SEM–EDX image of the coating with element mapping; e) Raman spectrum of the CHA coating.

EDX analysis and Raman characterization were performed on both microchannel surfaces (magnetic PDMS and glass coverslip). First, the average Ca/P atomic ratio measured along the microchannel was equal to 1.4 ± 0.1 on both surfaces. This value agrees with those reported in the literature for hydroxyapatite (HA) synthesized from SBF solution on bioactive surfaces, which is Ca-deficient HA (*i.e.* <1.67).[34,36,37] Raman analyses definitively confirmed the formation of HA with the bands at 437, 595 and 962 cm^{-1} assigned to $\nu_2(PO_4)$, $\nu_4(PO_4)$ and $\nu_1(PO_4)$ vibration modes, respectively (Fig. 2e).[38,39] The position of the $\nu_1(PO_4)$ band at 962 cm^{-1} is characteristic of crystalline HA; however, the slight dissymmetry of the band reveals the presence of a component at ≈950 cm^{-1} assigned to the presence of amorphous calcium phosphate.[40]

The broad band between 1000 and 1100 cm^{-1} combines the $\nu_1(CO_3)$ vibration mode at 1070 cm^{-1} with the $\nu_3(PO_4)$ vibration modes at 1048 cm^{-1} (medium intensity) and at 1075 cm^{-1} (weak intensity).[39] The amount of carbonate ions is difficult to estimate. A method was proposed in the literature based on the intensity ratio of $\nu_1(CO_3)$ and $\nu_1(PO_4)$ modes,[41] which leads to 5 wt%. Also the relative intensities between the $\nu_1(CO_3)$ and $\nu_3(PO_4)$ bands, with the maximum intensity for $\nu_1(CO_3)$, are consistent with what Kerssens *et al.*[42] have reported for a 6 wt% carbonate content. We can thus estimate the carbonate content to be around 5 wt%.

These results obtained on the CaP coating are consistent with the formation of a majority phase of carbonate-substituted HA (CHA) and a minority phase of amorphous calcium phosphate (ACP). These phases are similar to what is reported for the mineral part of RP,[12,43] which therefore validates our model.

The effect of the substrate on the crystallization of CaOx under flow

Several scenarios were selected to study the influence of CHA coating in the microchannel on CaOx crystallization (Fig. 3). The first scenario, SA, consisted of infusing for 2 h in the uncoated CHA microchannel aqueous calcium and oxalate solutions at concentrations corresponding to pathological hypercalciuria ($[Ca^{2+}]$ = 12.0 mM) and moderate hyperoxaluria ($[Ox^{2-}]$ = 0.4 mM).[44] This scenario was already studied in our previous report and served as a reference experiment.[24] The second scenario, SB, was similar to SA but the microchannel was coated with CHA. The total flow rate for the infused solutions for the two scenarios was equal to 0.20 µL min^{-1}, *i.e.* corresponding to 10 times the physiological flow inside one collecting duct of nephrons.[30] This flow rate was found to be a good compromise to observe

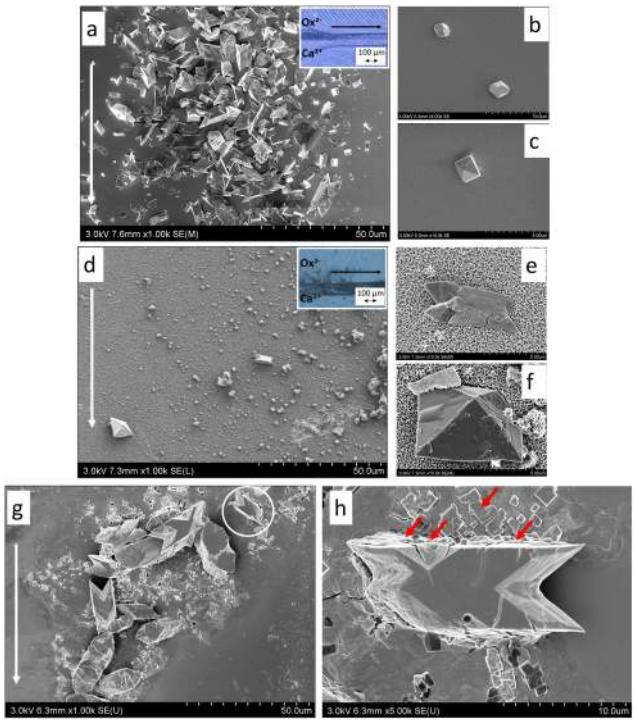

Fig. 3 Crystallization of CaOx in the microchannel after infusion of calcium and oxalate solutions. a–c) Scenario A (SA): uncoated channel – a) SEM-FEG image of the glass coverslip at 300 µm from the microchannel junction with an optical micrograph of the microchannel in the insert. b and c) SEM images of crystals collected at the end of the channel. d–f) Scenario B (SB): CHA coated channel – d) SEM-FEG image of the glass coverslip at 300 µm from the microchannel junction with an optical micrograph of the microchannel in the insert and enlarged images of crystals formed in the channel. g) Scenario C (SC): SEM-FEG image of the CHA coated coverslip at 300 µm from the microchannel junction. The white arrow in all figures indicates the direction of the flow. h) Magnification of the zone delimited by a white circle in image g). The red arrows indicate similar protuberance structures on the surface of CHA and CaOx crystals. The same images are provided at higher format in the ESI.†

the formation of CaOx crystals in a reasonable experiment time. After infusion of the precursor solutions into the microfluidic platform, the two parts (magnetic PDMS and glass coverslip) were separated and the precipitated CaOx crystals were characterized by SEM-FEG and Raman microscopy analysis. We found that they are mainly located at 300 µm from the microchannel junction (*i.e.* at the entrance to the 2.5 cm long microchannel), and consequently all optical and electron imaging was made at this position. In addition, the characterization was carried out on the glass slide which represents the upper part of the channel during the experiment allowing us to avoid any misinterpretations generated by deposition of CaOx crystals by gravity. The droplets at the end of the microfluidic channel that can mimic the urine of patients were characterized after drying by SEM in order to identify the nature of CaOx crystals formed in solution.

The *in situ* formation of CaOx crystals by co-mixing of calcium and oxalate aqueous solutions in the uncoated channel (scenario SA) resulted in the formation of two families of CaOx crystals (Fig. 3a). More specifically, we observed a majority (96%) of "boat-like" and "twinned" COM crystals with sizes equal to 6.7 ± 3.6 µm (measured on the (100) face) and 7.2 ± 3.6 µm (measured on the (010) face), and a minority (4%) of bipyramidal COD crystals with a size (measured along the *c* axis) equal to 4.1 ± 2.0 µm (see ESI,† Fig. ES1). These results are in good agreement with previously reported ones.[24] In the droplets collected at the end of the microchannel, SEM imaging showed the presence of COD crystals with two morphologies, "truncated octahedral" crystals with a size (measured on the (111) face) equal to 2.8 ± 1.7 µm (Fig. 3b) and bipyramidal crystals with a size (measured along the *c* axis) equal to 3.0 ± 1.9 µm (Fig. 3c). Although very few, the presence of only COD crystals in the droplets at the end of the channel is in complete agreement with the *in vivo* observations of Daudon *et al.*[44] made from the urine of patients with idiopathic hypercalciuria. The bipyramidal morphology is the classical one, indeed predicted for hydrated COD crystals by means of *ab initio* total crystal surface energy minimization.[45] Nevertheless, to the best of our knowledge, crystals with a truncated octahedral morphology were neither reported in batch crystallization, nor found in urine of patients.[44] However interestingly, some truncated morphologies have been theoretically predicted.[45] In addition, one important result from SA is that CaOx crystals formed in the microchannel (a large majority of COM) differ from those collected at the end of the channel (only COD). This may be explained by the difference in adhesiveness of COD and COM crystal faces, with COD crystals being less adhesive.[46] All these results may support again our previous hypothesis on two possible mechanisms for CaOx formation in the absence of CHA coating: (i) homogeneous nucleation in the flow of COD crystals and (ii) heterogeneous nucleation on the microchannel surfaces of COM crystals.[24]

The same analysis was conducted for SB to check the effect of CHA coating on CaOx crystallization under experimental conditions similar to SA. Surprisingly, the number of crystals was much lower than in SA (Fig. 3d) and no crystals were observed elsewhere in the channel (see ESI,† Fig. S2). The SEM images (Fig. 3d) showed the presence of only two types of single crystals, twinned COM and bipyramidal COD crystals. Moreover, unlike SA, no boat-like COM crystals were observed and the size of the bipyramidal COD crystal (measured along the *c* axis) was larger (11.4 ± 0.1 µm) while for the twinned COM crystal, the size was similar (7.8 ± 0.5 µm). At higher magnification (Fig. 3e and f), the crystalline particles deposited on the surface of CHA showed protuberances, apparently caused by engulfment of small, freshly nucleated CaOx crystals. Moreover the COM crystal appeared to lie on the surface (Fig. 3e), in contrast to the COD crystal (Fig. 3f) which was more embedded in the CHA layer. Analysis by SEM of the droplets collected at the exit of the microchannel in the case of SB showed the presence of a large aggregate with almost 15 µm diameter formed by

smaller particles (see ESI,† Fig. S3). The agglomerated precipitate is composed mainly of calcium and oxalate ions, as shown from EDX analysis. The concentration of calcium in the droplets collected at the exit for SA and SB was analyzed using calcium AAS spectroscopy. A similar average concentration value of calcium ions of about 8.1 mM was obtained in both cases. In addition, the SEM images of the coating after 2 h of flushing calcium oxalate solution showed little changes, supposing little dissolution of the CHA phase (see ESI,† Fig. S4). These results taken together demonstrate that calcium ions were consumed in majority by precipitation in the droplet outside the channel which can explain the small number of crystals observed inside the channel for SB. In mimetic batch solutions and urine samples, including under continuous flow, growth of CaOx crystals from supersaturated solutions containing HA seeds is proposed to occur by heterogeneous nucleation *via* macromolecules that promote the growth of CaOx.[27,47] However, in the case of SA despite a microfluidic configuration similar to that of SB, in the absence of macromolecules on the glass slide and after a relatively short contact time of 2 h, a high number of crystals was observed indicating that the surface of the substrate plays a role also in promoting the formation of CaOx crystals. These observations indicate that the formation of crystals on CHA is a complex time dependent phenomenon, which involves different stages: first, the diffusion of calcium and oxalate ions to the CHA/liquid interface, the dissolution of CHA at the CHA/liquid interface and finally the formation of CaOx on CHA. At the time scale of 2 h, the first two stages are probably limited due to the slow diffusion of ions to the solid/liquid interface and the low solubility of CHA. At the molecular level and for short residence times, we may assume the following hypothesis: the hydrogen bonds between the surface –OH of CHA and water are prominent rather than the –OH–oxalate bonds leading to very limited diffusion of oxalate molecules and solubility of CHA. For longer residence times, the oxalate molecules can reach the surface of CHA, facilitating the formation of CaOx by heterogeneous nucleation and/or through dissolution of Ca^{2+} from the apatite surface and its recrystallization to CaOx. Indeed when an aqueous oxalate solution ($[Ox^{2-}]$ = 0.4 mM) was injected at Q_i = 0.2 μL min^{-1} into the CHA-coated microchannel (scenario SC), strong dissolution of the HA coating (Fig. 3g and ESI,† S4) occurred after 24 h, confirming this hypothesis. In this case, only large (16–18 μm) boat-like and twinned COM crystals could be identified. These results indicate that the crystallization of CaOx crystals from the partially dissolved CHA coating can induce the exclusive formation of COM crystals with a specific morphology. A higher magnification on the surface of CHA in SC showed the presence of protuberances with an approximative edge of 0.6–1 μm (some indicated by an arrow in Fig. 3h) which sometimes fused together into larger multidimensional aggregates such as in the basal section of the COM crystals. This suggests that these small crystals are probably the first building blocks and can serve as starting points for the formation of the COM mesocrystals. In addition, higher magnification images (Fig. 3h and S5, ESI†) showed that they present the typical rhombohedral morphology of $CaCO_3$ calcite crystals.[48–50] The calcite crystals may have formed from CHA by dissolution crystallization. Indeed, it was shown that the presence of carbonates in solution increases the hydroxyapatite solubility.[13,51] To the best of our knowledge, the COM morphology obtained in SC has only been reported to date under batch crystallization in the presence of inhibitors of CaOx crystallization.[52,53] The presence of only COM crystals on the partially dissolved CHA coating is in accordance with the observations made by SEM on RP.[2,3,16,18] Tiselius *et al.*[5,54] proposed a sequence of events based on experimental and theoretical considerations for CaOx KS precipitation. Among the important steps that might lead to their formation, one concerns the dissolution of RP just before the appearance of the first CaOx nuclei. It was proposed that RP dissolution causes release of Ca^{2+} ions into the urine which increases the supersaturation of the medium and provides favourable conditions for the formation of CaOx nuclei on RP. Our experiments show that under supersaturated flow conditions, calcium ions are not the only limiting factor, but also oxalate ions. Indeed in addition to their possible role in the formation of CaOx on CHA, oxalate ions can induce the dissolution of the CHA coating which in a carbonated medium can generate calcite as a promoter of CaOx. At the exit of the microchannel (Fig. S6, ESI†) and after 24 h, large aggregates possibly generated from the dissolution of apatite and decorated with COM crystals are observed. In addition, small dots with a size of about 1 nm appear on the large aggregates, sometimes also attached to the COM crystals. A large population of these dot nanoparticles are observed to be also deposited on the glass coverslip, which also sometimes attach and merge with COM crystals inducing their growth. Such nanodots have also been observed by other groups during the growth of CaOx crystals including COM and they were attributed to amorphous CaOx crystals.[55,56]

Conclusions

We have developed a reversible microfluidic system and an easy flow assisted protocol for coating the channel with carbonated apatite (CHA) similar to the inorganic part of Randall's plaque. This system allowed us to investigate in a multi-scale approach the effect of carbonated apatite on the formation and crystal habits of CaOx crystals. Our results evidence the complexity of the crystal formation process with time and its dependency on the substrate nature and the solubility of CHA, as well as the important role of oxalate ions in inducing the formation of CaOx crystals on CHA. We also show that CaOx crystal growth can be promoted by calcium carbonate formed by dissolution of the apatite phase. Giving the versatility of the microsystem and the methodology, we intend in future work to increase the

complexity of the system in order to investigate the role of different organic compounds (lipids, *etc.*)[57] present in the apatite layer to better mimic the composition of Randall's plaque.

Author contributions

S. Bourg: investigation, methodology, formal analysis, visualization, writing – original draft. K. Rakotozandriny: investigation, methodology. Ivan T. Lucas: investigation. E. Letavernier: conceptualization, funding acquisition. C. Bonhomme: conceptualization, supervision, funding acquisition, project administration. F. Babonneau: conceptualization, supervision, visualization, writing – review & editing. A. Abou-Hassan: conceptualization, methodology, funding acquisition, supervision, visualization, writing – review & editing.

Conflicts of interest

There are no conflicts to declare.

Acknowledgements

This work was funded by Fondation de la Recherche Médicale (FRM, programme Chimie-Médecine 2018) that is greatly acknowledged. We would also like to thank Guillaume Laffite (IPGG, Paris) for technical support, as well as David Montero (FCMat, Sorbonne Université) and Isabelle Génois (LCMCP, Sorbonne Université) for the SEM experiments. A. A.-H acknowledges Nadine Nassif (LCMCP, Sorbonne Université) for fruitful discussions.

Notes and references

1 V. Romero, H. Akpinar and D. G. Assimos, *Rev. Urol.*, 2010, **12**, e86–e96.
2 D. Bazin, M. Daudon, C. Combes and C. Rey, *Chem. Rev.*, 2012, **112**, 5092–5120.
3 M. Daudon, O. Traxer, P. Jungers and D. Bazin, *AIP Conf. Proc.*, 2007, **900**, 26–34.
4 E. V. d. Perre, D. Bazin, V. Estrade, E. Bouderlique, K. M. Wissing, M. Daudon and E. Letavernier, *C. R. Chim.*, 2022, **25**, 373–391.
5 H. G. Tiselius, *Urol. Res.*, 2011, **39**, 231–243.
6 A. Randall, *Ann. Surg.*, 1937, **105**, 1009–1027.
7 S. R. Khan and B. K. Canales, *Urolithiasis*, 2015, **43**(1), 109–123.
8 R. S. Hsi, K. Ramaswamy, S. P. Ho and M. L. Stoller, *BJU Int.*, 2017, **119**, 177–184.
9 S. V. Wiener, S. P. Ho and M. L. Stoller, *Curr. Opin. Nephrol. Hypertens.*, 2018, **27**, 236–242.
10 S. R. Khan, B. K. Canales and P. R. Dominguez-Gutierrez, *Nat. Rev. Nephrol.*, 2021, **17**, 417–433.
11 X. Carpentier, D. Bazin, P. Jungers, S. Reguer, D. Thiaudière and M. Daudon, *J. Synchrotron Radiat.*, 2010, **17**, 374–379.
12 M. Daudon, D. Bazin and E. Letavernier, *Urolithiasis*, 2015, **43**(1), 5–11.
13 C. Gay, E. Letavernier, M.-C. Verpont, M. Walls, D. Bazin, M. Daudon, N. Nassif, O. Stéphan and M. de Frutos, *ACS Nano*, 2020, **14**, 1823–1836.
14 B. Xie, T. J. Halter, B. M. Borah and G. H. Nancollas, *Cryst. Growth Des.*, 2015, **15**, 204–211.
15 M. Hajir, R. Graf and W. Tremel, *Chem. Commun.*, 2014, **50**, 6534–6536.
16 I. Sethmann, G. Wendt-Nordahl, T. Knoll, F. Enzmann, L. Simon and H.-J. Kleebe, *Urolithiasis*, 2017, **45**, 235–248.
17 B. A. Sherer, L. Chen, M. Kang, A. R. Shimotake, S. V. Wiener, T. Chi, M. L. Stoller and S. P. Ho, *Acta Biomater.*, 2018, **71**, 72–85.
18 E. Letavernier, D. Bazin and M. Daudon, *C. R. Chim.*, 2016, **19**, 1456–1460.
19 R. L. Kuo, J. E. Lingeman, A. P. Evan, R. F. Paterson, J. H. Parks, S. B. Bledsoe, L. C. Munch and F. L. Coe, *Kidney Int.*, 2003, **64**, 2150–2154.
20 S. Kim and S. Takayama, *Kidney Res. Clin. Pract.*, 2015, **34**, 165–169.
21 N. Ashammakhi, K. Wesseling-Perry, A. Hasan, E. Elkhammas and Y. S. Zhang, *Kidney Int.*, 2018, **94**, 1073–1086.
22 M. J. Wilmer, C. P. Ng, H. L. Lanz, P. Vulto, L. Suter-Dick and R. Masereeuw, *Trends Biotechnol.*, 2016, **34**, 156–170.
23 G. Laffite, C. Leroy, C. Bonhomme, L. Bonhomme-Coury, E. Letavernier, M. Daudon, V. Frochot, J. P. Haymann, S. Rouzière, I. T. Lucas, D. Bazin, F. Babonneau and A. Abou-Hassan, *Lab Chip*, 2016, **16**, 1157–1160.
24 K. Rakotozandriny, S. Bourg, P. Papp, Á. Tóth, D. Horváth, I. T. Lucas, F. Babonneau, C. Bonhomme and A. Abou-Hassan, *Cryst. Growth Des.*, 2020, **20**, 7683–7693.
25 P. Papp, S. Bourg, M. Emmanuel, Á. Tóth, A. Abou-Hassan and D. Horváth, *Cryst. Growth Des.*, 2023, **23**, 8116–8123.
26 F. Gombedza, S. Evans, S. Shin, E. Awuah Boadi, Q. Zhang, Z. Nie and B. C. Bandyopadhyay, *Sci. Rep.*, 2019, **9**, 875.
27 C. A. Kuliasha, D. Rodriguez, A. Lovett and L. B. Gower, *CrystEngComm*, 2020, **22**, 1448–1458.
28 A. C. Lovett, S. R. Khan and L. B. Gower, *Urolithiasis*, 2019, **47**, 321–334.
29 A. L. O'Kell, A. C. Lovett, B. K. Canales, L. B. Gower and S. R. Khan, *Urolithiasis*, 2019, **47**, 335–346.
30 In *The Kidney*, ed. P. D. Vize, A. S. Woolf and J. B. L. Bard, Academic Press, San Diego, 2003, pp. 493–519, DOI: **10.1016/B978-012722441-1/50031-2**.
31 Q. Liu, J. Ding, F. K. Mante, S. L. Wunder and G. R. Baran, *Biomaterials*, 2002, **23**, 3103–3111.
32 Z. Wei, P. K. Amponsah, M. Al-Shatti, Z. Nie and B. C. Bandyopadhyay, *Lab Chip*, 2012, **12**, 4037–4040.
33 T. Kokubo, *Biomaterials*, 1991, **12**, 155–163.
34 M. Tanahashi and T. Matsuda, *J. Biomed. Mater. Res.*, 1997, **34**, 305–315.
35 T. Kokubo and H. Takadama, *Biomaterials*, 2006, **27**, 2907–2915.
36 P. Li, C. Ohtsuki, T. Kokubo, K. Nakanishi, N. Soga, T. Nakamura and T. Yamamuro, *J. Am. Ceram. Soc.*, 1992, **75**, 2094–2097.

37 T. Kasuga, Y. Hosoi, M. Nogami and M. Niinomi, *J. Am. Ceram. Soc.*, 2001, **84**, 450–452.
38 S. Koutsopoulos, *J. Biomed. Mater. Res.*, 2002, **62**, 600–612.
39 I. A. Karampas and C. G. Kontoyannis, *Vib. Spectrosc.*, 2013, **64**, 126–133.
40 J. A. Stammeier, B. Purgstaller, D. Hippler, V. Mavromatis and M. Dietzel, *MethodsX*, 2018, **5**, 1241–1250.
41 G. Penel, C. Delfosse, M. Descamps and G. Leroy, *Bone*, 2005, **36**, 893–901.
42 M. M. Kerssens, P. Matousek, K. Rogers and N. Stone, *Analyst*, 2010, **135**, 3156–3161.
43 L. Estepa and M. Daudon, *Biospectroscopy*, 1997, **3**, 347–369.
44 M. Daudon, E. Letavernier, V. Frochot, J.-P. Haymann, D. Bazin and P. Jungers, *C. R. Chim.*, 2016, **19**, 1504–1513.
45 T. Debroise, T. Sedzik, J. Vekeman, Y. Su, C. Bonhomme and F. Tielens, *Cryst. Growth Des.*, 2020, **20**, 3807–3815.
46 X. Sheng, T. Jung, J. A. Wesson and M. D. Ward, *Proc. Natl. Acad. Sci. U. S. A.*, 2005, **102**, 267–272.
47 J. L. Meyer, J. H. Bergert and L. H. Smith, *Clin. Sci. Mol. Med.*, 1975, **49**, 369–374.
48 S. Kim and C. B. Park, *Biomaterials*, 2010, **31**, 6628–6634.
49 J. Aizenberg, G. Lambert, S. Weiner and L. Addadi, *J. Am. Chem. Soc.*, 2002, **124**, 32–39.
50 M.-K. Jo, Y. Oh, H. J. Kim, H. L. Kim and S. H. Yang, *Cryst. Growth Des.*, 2020, **20**, 560–567.
51 H. Pan and B. W. Darvell, *Cryst. Growth Des.*, 2010, **10**, 845–850.
52 Y. V. Taranets, I. M. Pritula, O. N. Bezkrovnaya, P. V. Mateychenko, D. S. Sofronov and A. N. Puzan, *Cryst. Res. Technol.*, 2018, **53**, 1700133.
53 J. Yu, H. Tang and B. Cheng, *J. Colloid Interface Sci.*, 2005, **288**, 407–411.
54 H. G. Tiselius, B. Lindbäck, A. M. Fornander and M. A. Nilsson, *Urol. Res.*, 2009, **37**, 181–192.
55 J. Ihli, Y.-W. Wang, B. Cantaert, Y.-Y. Kim, D. C. Green, P. H. H. Bomans, N. A. J. M. Sommerdijk and F. C. Meldrum, *Chem. Mater.*, 2015, **27**, 3999–4007.
56 J. Zhang, L. Wang, W. Zhang and C. V. Putnis, *Cryst. Growth Des.*, 2021, **21**, 683–691.
57 A. Dey, P. H. Bomans, F. A. Müller, J. Will, P. M. Frederik, G. de With and N. A. Sommerdijk, *Nat. Mater.*, 2010, **9**, 1010–1014.

Electronic Supplementary Information

Confining calcium oxalate crystal's growth in carbonated apatite-coated microfluidic channel to better understand the role of Randall's plaque in kidney stone formation

Samantha Bourg,[a] Karol Rakotozandriny,[a,b] Ivan T. Lucas,[c] Emmanuel Letavernier,[d] Christian Bonhomme,[b] Florence Babonneau,[b] and Ali Abou-Hassan*[a,e]

Ali.abou_hassan@sorbonne-universite.fr

Table 1: Chemical composition in Na^+, K^+, Mg^{2+}, Ca^{2+}, Cl^-, HCO_3^-, HPO_4^{2-} and SO_4^{2-} ions of 1.5 SBF solution buffered at pH 7.4 with 10 mM Tris-HCl.

Ions	Na^+	K^+	Mg^{2+}	Ca^{2+}	Cl^-	HCO_3^-	HPO_4^{2-}	SO_4^{2-}
ion concentrations (mmol/L)	213.0	7.5	2.3	3.8	221.7	6.3	1.5	0.8

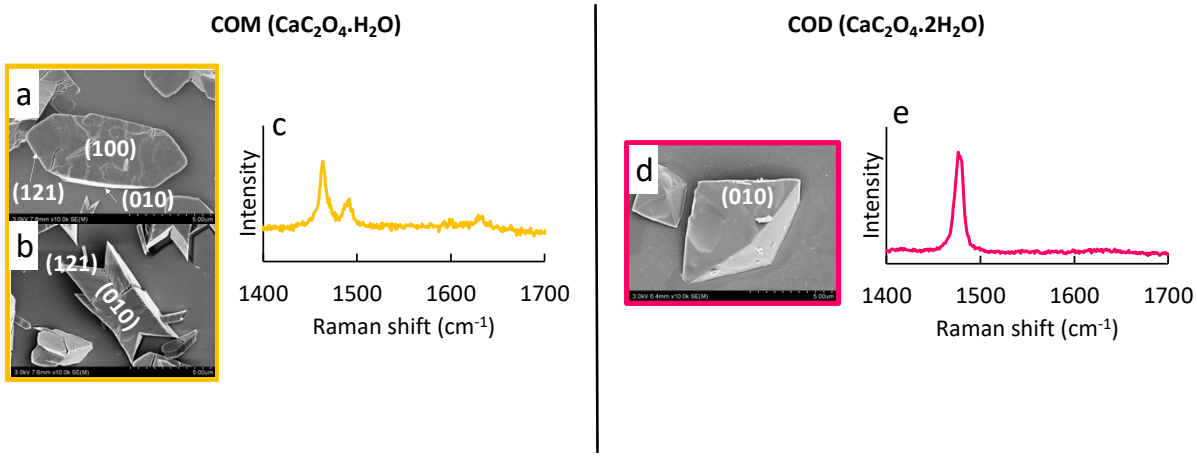

Fig. S1: a,b) SEM-FEG images of COM crystals and d) COD crystals with their respective Raman spectra

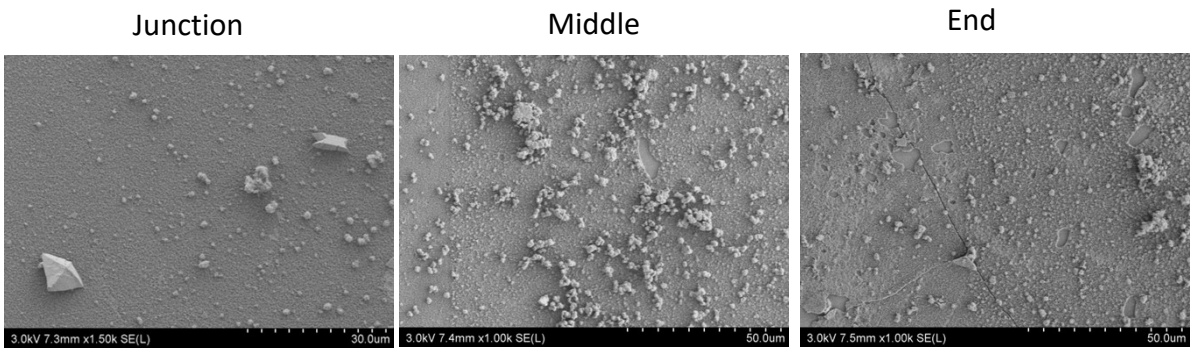

Fig. S2: SEM images of CHA coating at different positions in the channel after perfusion of oxalate and calcium solutions for 2h (SB)

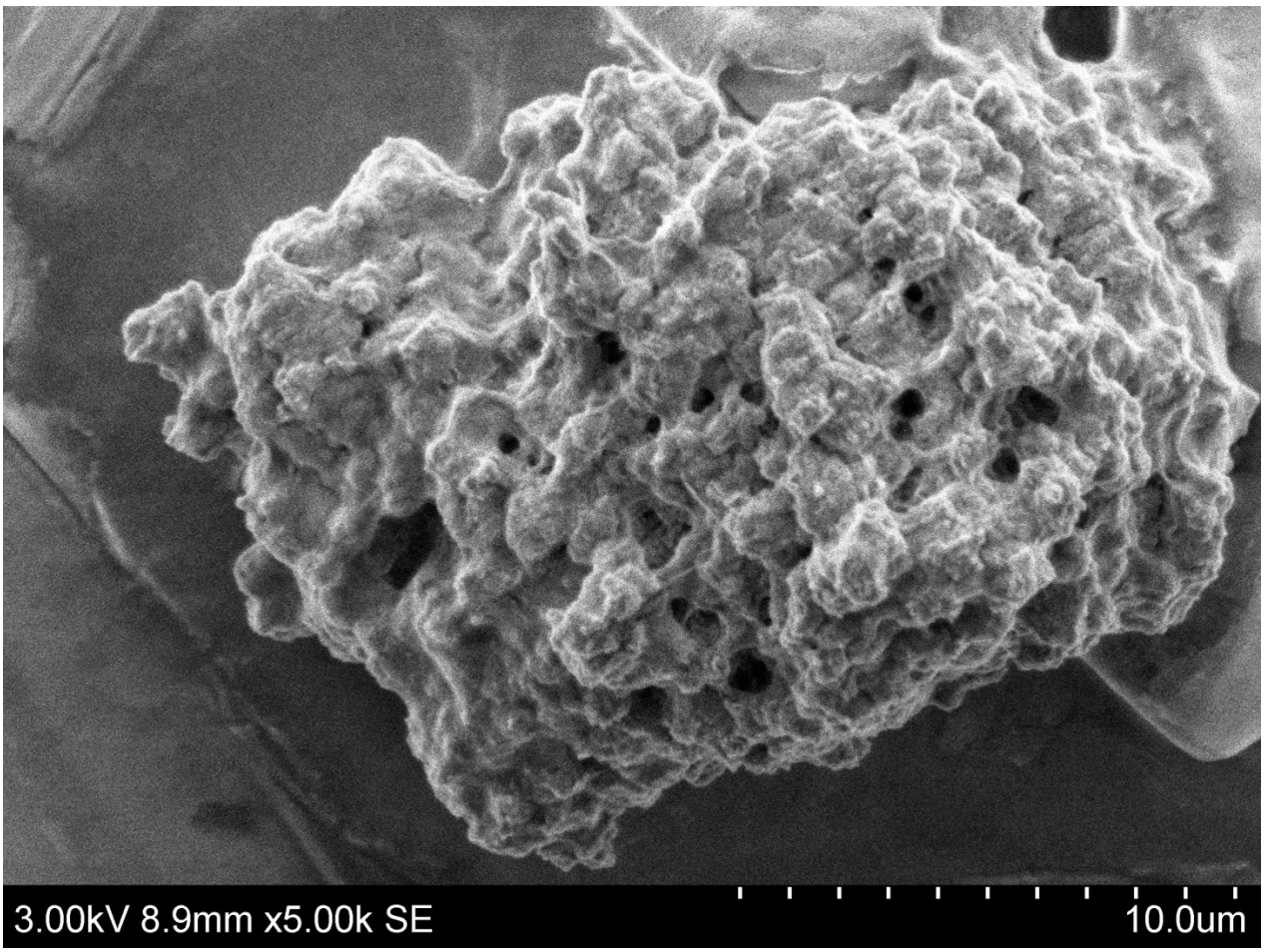

Fig. S3: SEM image showing the precipitate formed at the outlet of the microchannel after perfusion of oxalate and calcium solutions for 2h (SB)

Fig. S4: SEM-FEG images of the initial CHA substrate and at the end of the experiment for SB and SC

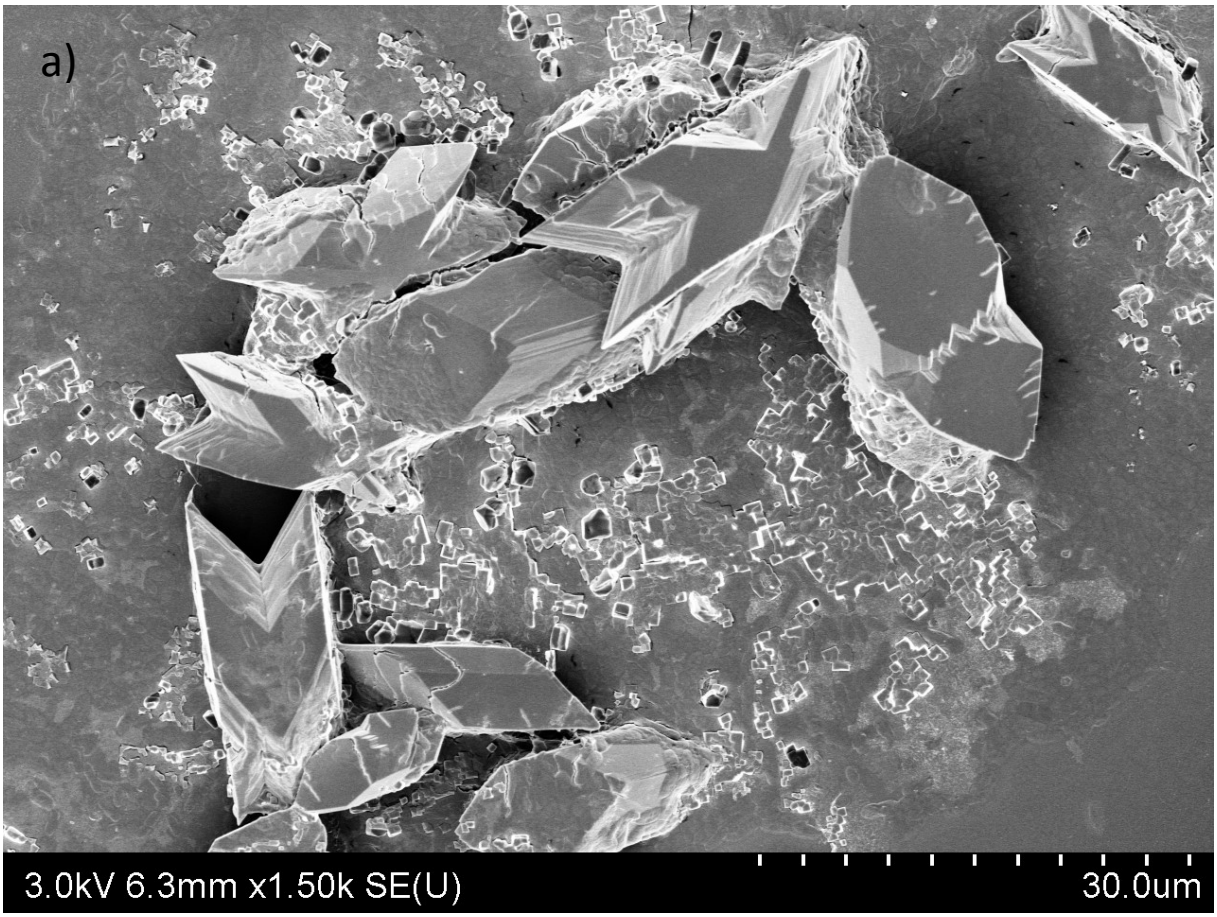
a)
3.0kV 6.3mm x1.50k SE(U)
30.0um

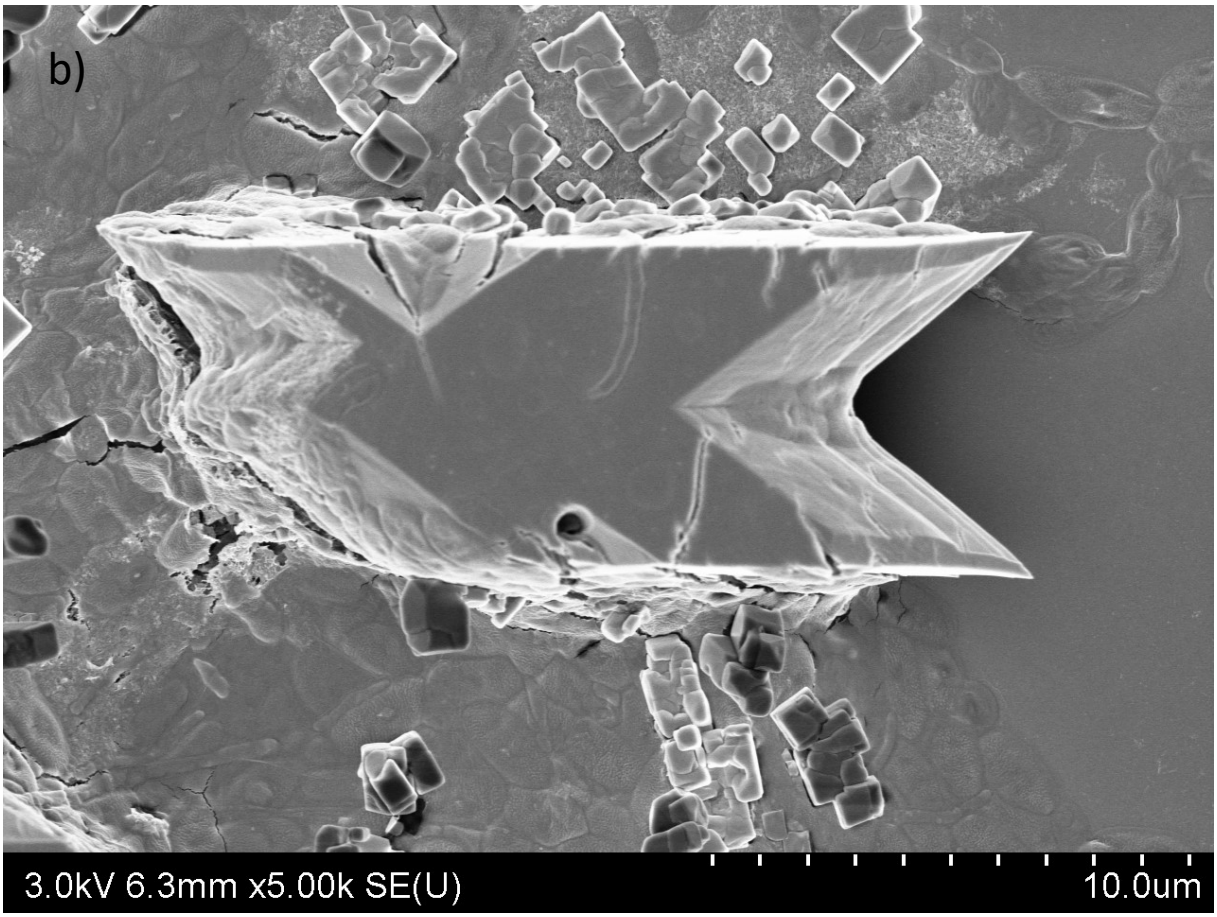
b)
3.0kV 6.3mm x5.00k SE(U)
10.0um

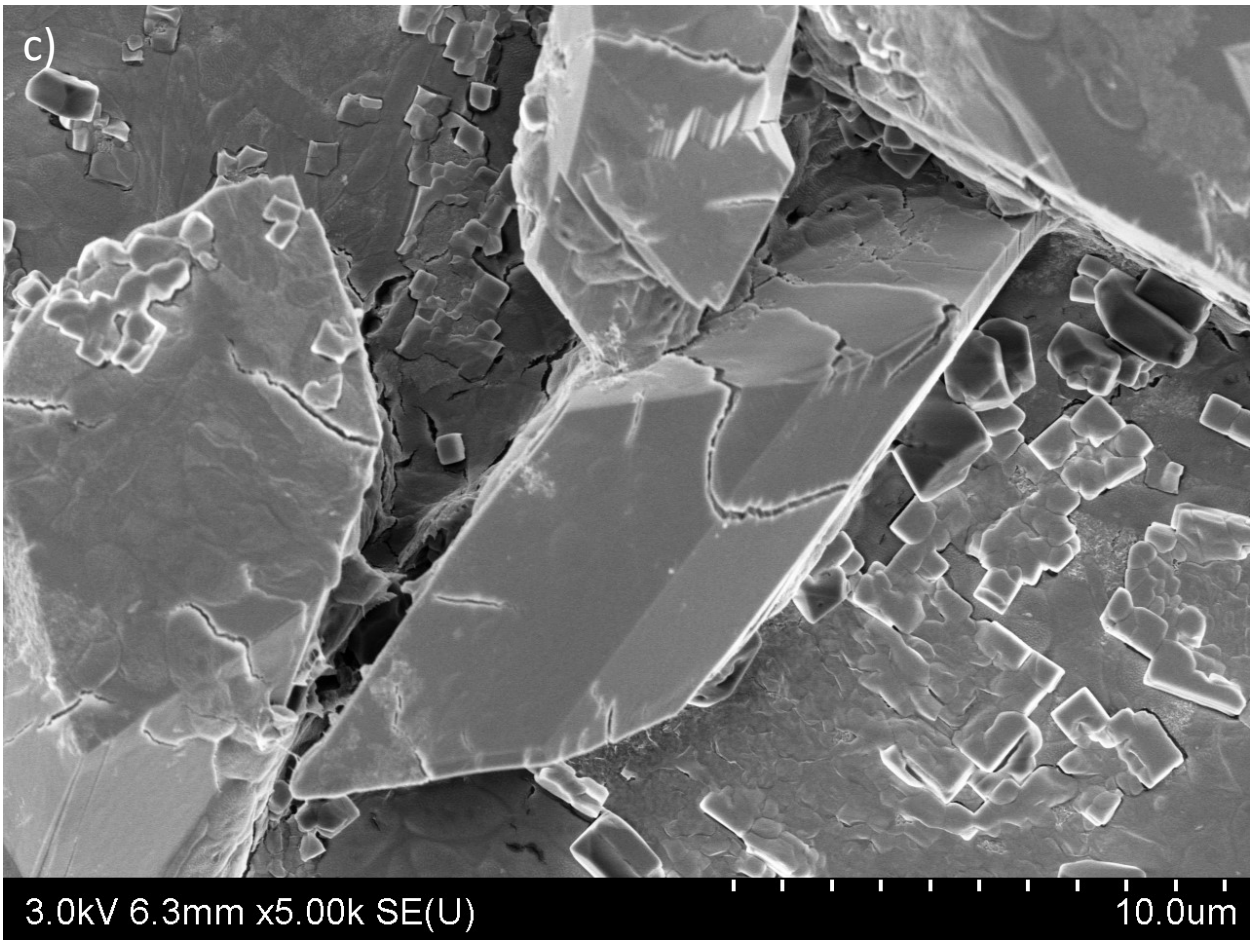

Fig. S5: a-c) Crystallization of CaOx in the microchannel after infusion of calcium and oxalate solutions on CHA for 2h (SB)

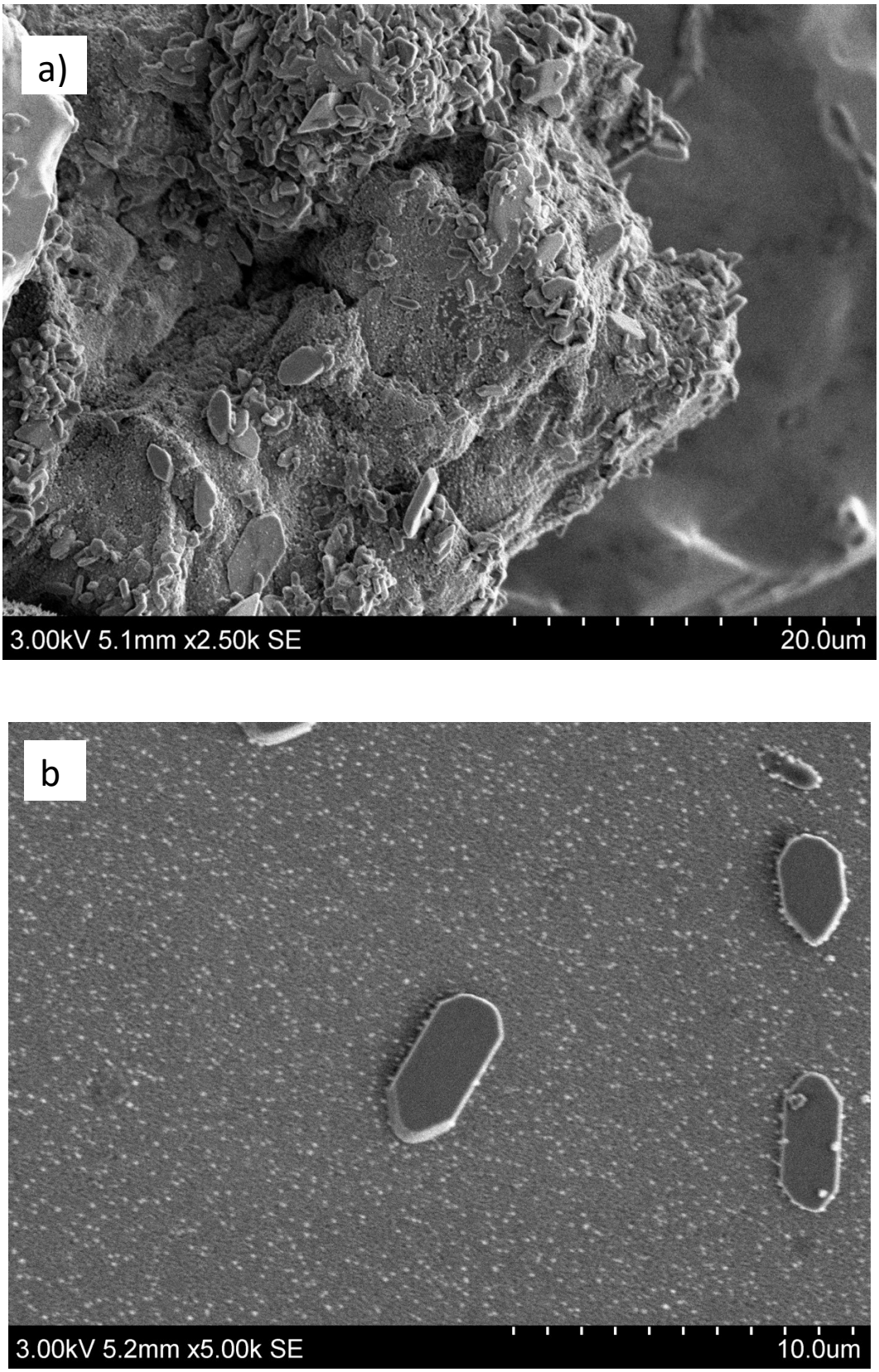

Fig. S6: a,b) Crystallization of CaOx at the outlet of the microchannel after infusion of oxalate solutions on CHA for 24h (SC)